

## RESEARCH ARTICLE

## CANCER

# Cancer cells use self-inflicted DNA breaks to evade growth limits imposed by genotoxic stress

Brian D. Larsen<sup>1</sup>, Jan Benada<sup>1</sup>, Philip Yuk Kwong Yung<sup>2†</sup>, Ryan A. V. Bell<sup>3†</sup>, George Pappas<sup>4†</sup>, Vaclav Urban<sup>5</sup>, Johanna K. Ahlskog<sup>1</sup>, Tia T. Kuo<sup>1</sup>, Pavel Janscak<sup>5,6</sup>, Lynn A. Megeney<sup>3</sup>, Simon J. Elsäßer<sup>2</sup>, Jiri Bartek<sup>2,4,5</sup>, Claus S. Sørensen<sup>1\*</sup>

Genotoxic therapy such as radiation serves as a frontline cancer treatment, yet acquired resistance that leads to tumor reoccurrence is frequent. We found that cancer cells maintain viability during irradiation by reversibly increasing genome-wide DNA breaks, thereby limiting premature mitotic progression. We identify caspase-activated DNase (CAD) as the nuclease inflicting these *de novo* DNA lesions at defined loci, which are in proximity to chromatin-modifying CCCTC-binding factor (CTCF) sites. CAD nuclease activity is governed through phosphorylation by DNA damage response kinases, independent of caspase activity. In turn, loss of CAD activity impairs cell fate decisions, rendering cancer cells vulnerable to radiation-induced DNA double-strand breaks. Our observations highlight a cancer-selective survival adaptation, whereby tumor cells deploy regulated DNA breaks to delimit the detrimental effects of therapy-evoked DNA damage.

Genotoxic cancer therapy inactivates and kills cancer cells by inflicting extensive DNA damage. Radiation therapy (RT) is the most broadly applied genotoxic challenge in standard-of-care oncological treatment. The deposition of energy as radiation passes through the genetic material triggers extensive DNA lesions often in the form of double-strand breaks (DSBs), single-stranded breaks (SSBs), and interstrand cross-links (1). The extent of this damage can present an insurmountable barrier to cellular fitness, triggering cell death or cell cycle withdrawal. Facilitating the DNA damage response (DDR) and lesion repair while avoiding cell death and cell cycle blockage is critical for cell survival after RT. Clinically, resistance to RT remains a considerable obstacle to effective tumor control, as the cancer cells deploy an arsenal of mechanisms, still incompletely understood, to mitigate the effects of RT (1).

Irradiated normal cells halt progression in the G<sub>1</sub> phase of the cell cycle by activation of p53 and pRb, which are key factors regulating cell cycle checkpoints. However, these factors are commonly inactivated in solid cancers,

leading to G<sub>1</sub> checkpoint deficiency. Combined with oncogene-driven premature S-phase entry, this scenario evokes replication stress and enhanced chromosomal damage that requires efficient repair should the cell yield viable progenies when it divides (2). Hence, cancer cells particularly rely on the G<sub>2</sub> cell cycle checkpoint, preventing entry into mitosis with unrepaired DNA breaks (3). In addition, studies following the dynamics of RT-induced DNA lesions have indicated the presence of a temporally distinct and unexplained secondary wave of DNA breaks (4). To identify potential nuclease regulators of the G<sub>2</sub> cell cycle checkpoint after radiation, we screened a library targeting the known human nucleases in cancer cells (fig. S1) (5). The primary candidate emerging from this screen was RBBP8 (CtIP), an established DDR and G<sub>2</sub> checkpoint factor (6). Unexpectedly, a second robust target from this screen was DFFB (also known as caspase-activated DNase or CAD), a factor previously unassociated with DDR or cell cycle checkpoint control. CAD is the nuclease implicated in DNA fragmentation during apoptotic cell death as the effector of caspase signaling cascades (7, 8). Caspase-mediated cleavage of CAD's chaperone and inhibitor, ICAD (inhibitor of CAD), facilitates the dimerization of CAD, giving rise to the hallmark DNA fragmentation seen in apoptosis (8).

CAD-inflicted DNA breaks and the ensuing DDR signals have also been implicated as inductive cues for a number of nonapoptotic cell fate states and transitions (9–15). Intriguingly, RT-induced DNA lesions encompass a temporally distinct and mechanistically unexplained secondary wave of DNA breaks (4). Together, these observations led us to hypothesize that

CAD might be responsible for inflicting these delayed post-irradiation DNA breaks to exert checkpoint control, potentially providing a mechanism of radioresistance.

## CAD promotes a wave of endogenous DNA breaks after exogenous DNA damage

To address the nature of the endogenous DNA breaks that have been reported to appear after exposure to ionizing radiation (IR), we irradiated human wild-type and CAD null (KO) colorectal cancer-derived HCT116 cells and measured the extent of DNA damage by alkaline single-cell gel electrophoresis (Comet assay) (Fig. 1A and fig. S2A). We did not observe any initial differences in DNA lesion accumulation between wild-type and CAD KO cells after exposure to IR. Further, the progressive reduction in DNA damage burden through active DNA repair was comparable between wild-type and CAD KO cells. However, consistent with recent observations (4), we detected a secondary accumulation of DNA lesions in wild-type cells that was prominent 24 hours after IR (Fig. 1A). The extent of DNA breakage was dependent on IR dosage (Fig. 1B). DNA break accumulation at 24 hours was largely dependent on the nuclease activity of CAD (Fig. 1C). These CAD-dependent breaks were observed in a panel of human malignant cell lines, but not in cells of nonmalignant origin (Fig. 1D and fig. S2B). To support this finding, we used *in situ* nick translation (ISNT) to quantify DNA breaks (15). This approach revealed a similar CAD-dependent elevation in DNA breaks at 24 hours after IR (Fig. 1E). CAD is normally present in a protein complex with ICAD, which also acts as a chaperone required to properly fold CAD (8). Accordingly, we recapitulated our observations in cells lacking ICAD, where the expression of CAD is lost (fig. S2, C and D). Further, extensive DNA DSB formation could not account for the prevalent CAD-dependent DNA breaks seen by the alkaline approach, although a discrete population of DNA DSBs might exist (fig. S2E).

PARP-1 [poly(ADP-ribose)polymerase-1] serves as a sensor of DNA lesions that triggers DNA repair and was previously implicated in the repair of DNA breaks after IR (4, 16). Consistent with the appearance of DNA breaks at 24 hours after IR, we observed active ongoing DNA repair signaling, as evident from elevated poly(ADP-ribose) quantities (fig. S3A). Inhibition of PARP with 4-ANI, a strong enzymatic-activity inhibitor with only weak PARP-trapping activity, led to an elevation in DNA breaks even when the inhibitor was added for the last 2 hours of the 24-hour period after IR (fig. S3B) (17). The elevated PARP activity and increased DNA breaks upon PARP inhibition were both dependent on CAD (fig. S3, A and B).

The extent of single-stranded DNA (ssDNA) at 24 hours after IR was also monitored by

<sup>1</sup>Biotech Research and Innovation Centre, University of Copenhagen, 2200 N Copenhagen, Denmark. <sup>2</sup>Science for Life Laboratory, Division of Genome Biology, Department of Medical Biochemistry and Biophysics, Karolinska Institutet, 17165 Stockholm, Sweden. <sup>3</sup>Sprott Centre for Stem Cell Research, Ottawa Hospital Research Institute and Departments of Medicine and Cellular and Molecular Medicine, University of Ottawa, Ottawa, Ontario K1H 8L6, Canada. <sup>4</sup>Danish Cancer Society Research Center, 2100 Copenhagen, Denmark. <sup>5</sup>Institute of Molecular Genetics, Academy of Sciences of the Czech Republic, 143 00 Prague, Czech Republic. <sup>6</sup>Institute of Molecular Cancer Research, University of Zurich, 8057 Zurich, Switzerland.

\*Corresponding author. Email: claus.storgaard@bric.ku.dk

†These authors contributed equally to this work.

native bromodeoxyuridine (BrdU) and replication protein A (RPA) foci formation. Both approaches demonstrated elevated numbers of ssDNA foci in the control irradiated cells but not in cells deficient for CAD/ICAD at this time point (fig. S3, C to H). In support of this observation, RPA foci formation at 24 hours could be restored by transient expression of wild-type CAD but not a nuclease-dead (ND) CAD variant (fig. S3I).

We postulated that elevation of DNA break quantities could signal a delayed chromatin response after IR. Consistent with this hypothesis, the maintenance of KAP1 phosphorylation, a chromatin marker of ongoing DDR, was dependent on CAD (fig. S4, A to C) (18). In addition to IR, we have observed a similar CAD-dependent signaling after doxorubicin-induced genotoxic damage, which also inflicts DNA DSBs (fig. S4, D to F). Collectively, these observations suggest that CAD nuclease induces self-inflicted DNA breaks in cancer cells. Canonically, caspase-3-mediated cleavage of ICAD releases CAD from inhibition, allowing for CAD dimerization. This positions each nuclease cleft in parallel across a DNA double-strand segment. Each nuclease cleft creates a single-stranded break in DNA that together produce a DSB (8). Notably, CAD can also inflict DNA nicks during early apoptosis and skeletal muscle differentiation (19, 20). However, it has been reported that IR exposure of solid tumor cells does not elicit a robust caspase response (21). Here, we did not observe evidence of caspase-3 activation or proteolytic processing of ICAD after IR. Further, inhibition of pan-caspase activity did not affect the observed induction of DNA breaks, suggesting a noncanonical activation of CAD after IR (fig. S4, C, G, H, and I).

### Chromatin recruitment of CAD and ICAD

We observed that both CAD and ICAD were recruited to the chromatin fraction of IR-treated cells (Fig. 2A and fig. S5A). ICAD interaction with CAD typically limits recruitment of the nuclease to DNA (22). However, the nuclease cleft of CAD is exposed in the CAD/ICAD heterodimer; thus, chromatin interactions could produce DNA nicks (22). To address whether chromatin recruitment of CAD/ICAD was sufficient to induce DNA breaks, we used the chromatin tethering model of U2OS 263 cells that harbors an integrated LacO array (23). Expressed mCherry-LacR-ICAD was correctly recruited to the LacO array and could recruit a green fluorescent protein (GFP)-tagged CAD to this site (fig. S5B). Analysis of the mCherry-LacR-ICAD tethered arrays in comparison to the empty mCherry-LacR construct revealed an induction of DNA breaks, as characterized by the creation of 3'-OH DNA ends that could be readily detected by terminal deoxynucleotidyl transferase end labeling

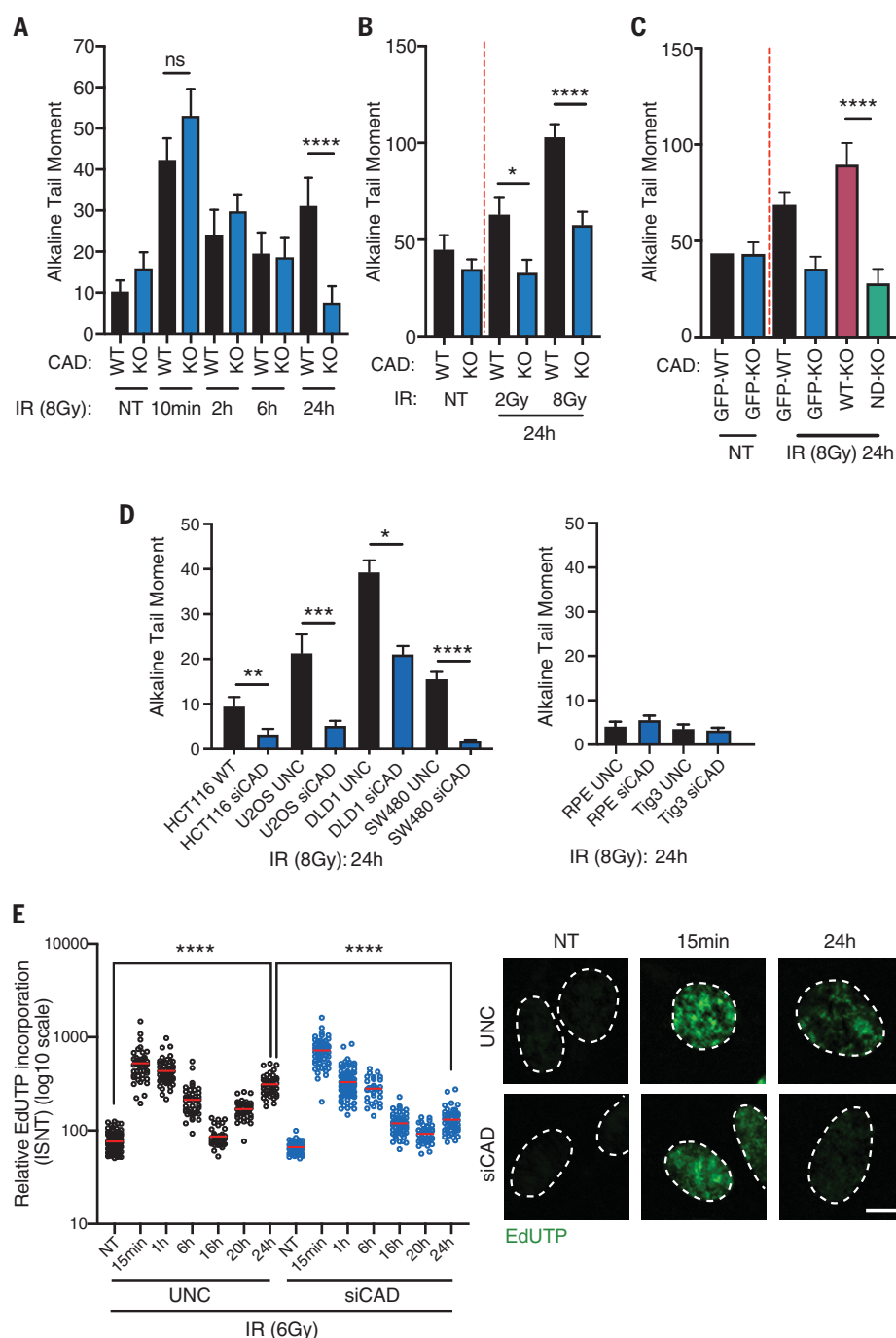


**Fig. 1. CAD promotes self-inflicted DNA breaks after IR.** (A) Alkaline Comet assay of HCT116 wild-type (WT) and CAD KO cells upon 8 Gy of IR; a representative dataset is presented. Data are means  $\pm$  SEM;  $N = 3$ ,  $n > 100$ . \*\*\*\*  $P < 0.0001$  (Kruskal-Wallis multiple-comparisons test); ns, not significant. (B) Alkaline Comet assay of HCT116 WT and CAD KO cells upon 2 or 8 Gy of IR; a representative dataset is presented. Data are means  $\pm$  SEM;  $N = 3$ ,  $n > 100$ . \*  $P = 0.0147$ , \*\*\*\*  $P < 0.0001$  (Kruskal-Wallis multiple-comparisons test). (C) WT CAD, but not a ND CAD, restores DNA breaks as measured by the Alkaline Comet assay 24 hours after 8 Gy of IR; a representative dataset is presented. Data are means  $\pm$  SEM;  $N = 3$ ,  $n > 100$ . \*\*\*\*  $P < 0.0001$  (Kruskal-Wallis multiple-comparisons test). (D) DNA break quantities 24 hours after 8 Gy of IR in cancer cell lines HCT116, U2OS, DLD-1, and SW480 and in noncancer cell lines RPE1 and Tig3 in control (UNC) or CAD-depleted cells (siCAD); a representative dataset is presented. Data are means  $\pm$  SEM;  $N = 3$ ,  $n > 100$ . \*  $P = 0.0337$ , \*\*  $P = 0.074$ , \*\*\*  $P = 0.0001$ , \*\*\*\*  $P < 0.0001$  (Kruskal-Wallis multiple-comparisons test). (E) Relative ethynyl-deoxyuridine triphosphate incorporation into DNA breaks using ISNT in U2OS (control or CAD-depleted) cells upon 6 Gy of IR; a representative dataset is presented. Scale bar, 10  $\mu$ m. Data are means  $\pm$  SEM;  $N = 3$ ,  $n > 30$ . \*\*\*\*  $P < 0.001$  (unpaired Student's  $t$  test).

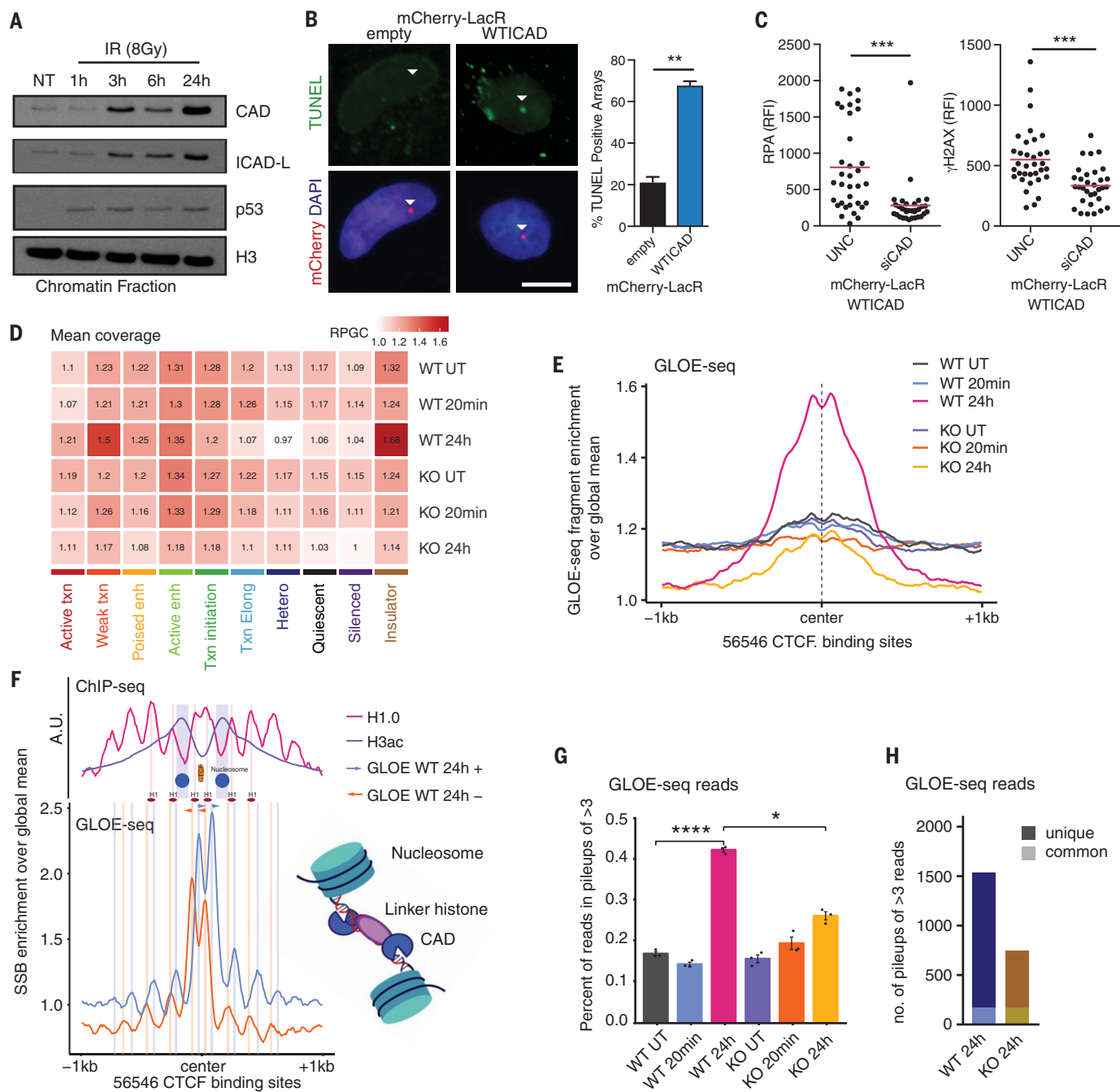


**Fig. 2. CAD/ICAD chromatin recruitment inflicts DNA breaks at defined genomic elements.** (A) Immunoblotting of chromatin fraction of HCT116 cells upon 8 Gy of IR. Recruitment of p53 was used as a positive control; H3 was used as a loading control. (B) TUNEL end labeling of 3'-OH indicates the formation of DNA breaks in mCherry-LacR-ICAD transfected cells. Scale bar, 10  $\mu$ m. Data are means  $\pm$  SEM;  $N = 3$ ,  $n > 50$ .  $^{**}P < 0.005$  (unpaired Student's  $t$  test). (C) Knockdown of CAD in mCherry-LacR-ICAD transfected cells reduces RPA and  $\gamma$ -H2AX.  $N = 3$ ,  $n > 20$ .  $^{***}P < 0.001$  (unpaired Student's  $t$  test). RFI, relative fluorescence intensity. (D) Genome-wide landscape of SSBs in HCT116 WT or CAD KO cells, before, 20 min after, and 24 hours after 8 Gy of IR. Average GLOE-seq read densities combined from three independent replicates are summarized over functionally distinct genomic regions as defined by a 10-state ChromHMM genome annotation. Elong, elongation; Enh, enhancer; Hetero, heterochromatin; Txn, transcription; UT, untreated. (E) SSB distribution around 56,546 CTCF binding sites in HCT116 cells. Average profiles from paired-end GLOE-seq fragments are plotted. (F) Footprint

analysis of core and linker histones and SSBs around 56,546 CTCF binding sites in HCT116 cells. Linker histone H1.0 genomic occupancies are well positioned with a  $\sim 160$ -bp periodicity flanking the central CTCF binding site. GLOE-seq nick sites are piled up separately for the plus and minus strand. SSBs peak symmetrically and in a defined direction adjacent to the linker histone. (G) Three GLOE-seq replicates of each condition were filtered for duplicates and artificially over-represented regions, downsampled to the same sequencing depth (2 Mio reads), and examined for pileups of three or more unique forward reads within a 20-bp window indicating exact or near-exact coincidence of SSBs in multiple individual cells, thus "hypersensitive" nick sites. Data are means  $\pm$  SEM.  $^{*}P = 0.011$ ,  $^{****}P = 5.6 \times 10^{-5}$  (Student's  $t$  test and Bonferroni correction). (H) A comprehensive list of pileups was generated from pooled replicates. Each pileup region was matched against the pileup regions of the other five conditions to exclude common treatment-independent hypersensitive nick sites. WT cells showed more than 1000 unique hypersensitive nick sites as compared to CAD KO cells.

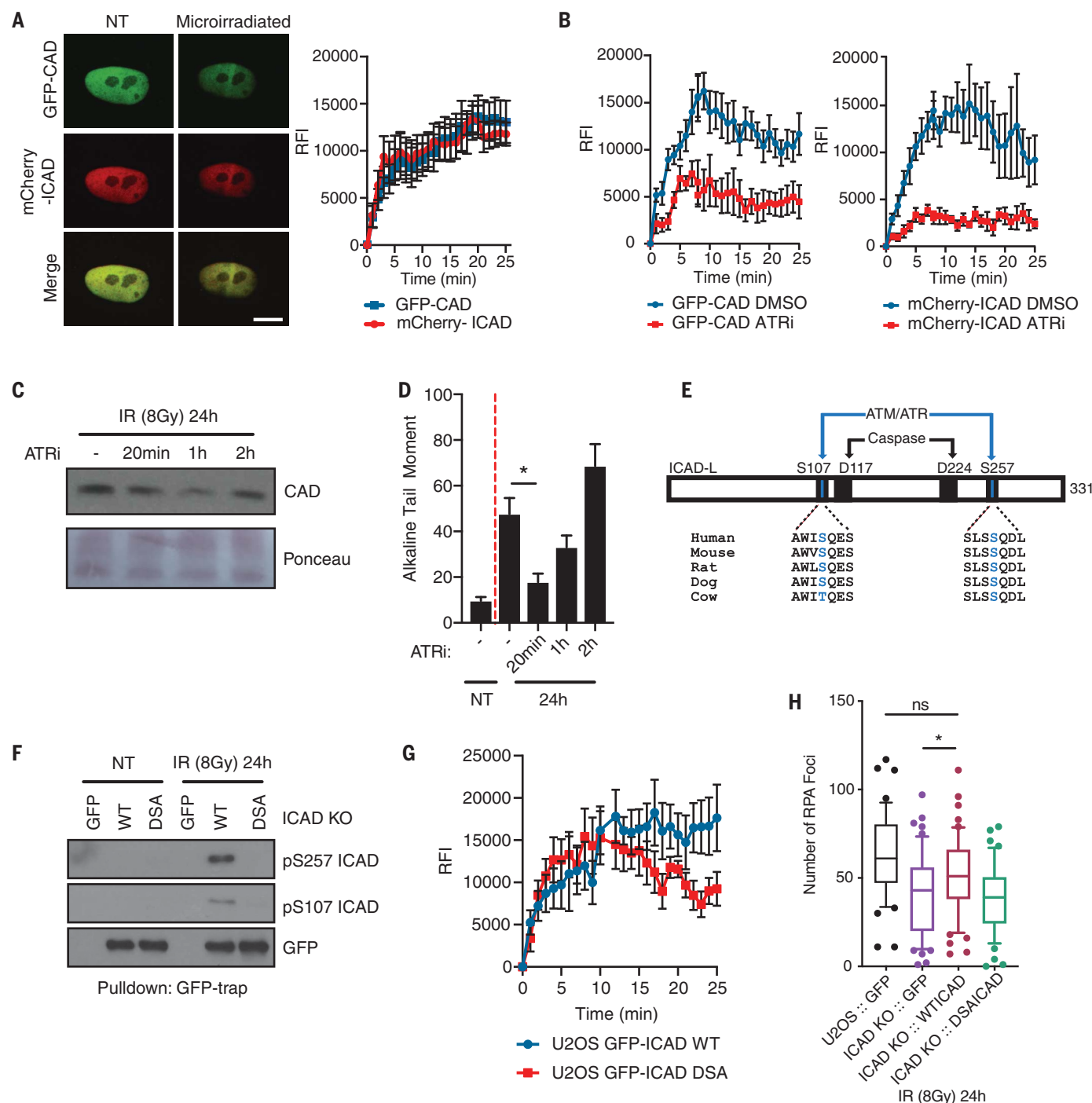


**Fig. 3. ATM/ATR signaling to ICAD regulates CAD-induced DNA breaks after IR.** (A) U2OS cells expressing mCherry-ICAD and GFP-CAD were microirradiated and imaged every minute for 25 min. Scale bar, 10  $\mu$ m. Data are means  $\pm$  SEM; cells per biological replicate,  $n = 6$ ; biological replicates,  $N = 3$ . (B) Recruitment of CAD and ICAD to microirradiated laser stripes after inhibition of ATR. Conditions as in (A), except that ATRi AZ20 was added 20 min before microirradiation. RFI, SEM, replicates, and  $n/N$  are the same as in (A). (C) ATR inhibition (AZ20) for the indicated times prior to collection affects chromatin recruitment of CAD at 24 hours after 8 Gy of IR in HCT116 cells. (D) DNA break measurements under conditions like those in (C) in HCT116 cells. Data are means  $\pm$  SEM;  $N = 3$ ,  $n > 100$ .  $*P < 0.0443$  (Kruskal-Wallis multiple-comparisons test). (E) Protein sequence analysis

(Clustal Omega) of ICAD indicates two conserved ATM/ATR SQ phosphorylation motifs. (F) ICAD is phosphorylated at Ser<sup>107</sup> and Ser<sup>257</sup> after IR. ICAD KO U2OS cells expressing GFP, WT ICAD, or DSA ICAD were irradiated (8 Gy) and GFP-tagged proteins enriched by GFP trap. Immunoblotting with phospho-specific antibodies to Ser<sup>107</sup> and Ser<sup>257</sup> on ICAD. (G) DSA-ICAD is not stably recruited to laser-microirradiated damage. U2OS cells expressing GFP-WT ICAD or GFP-DSA ICAD were laser-microirradiated and imaged every minute for 25 min. Data are means  $\pm$  SEM; cells per biological replicate,  $n = 7$ ; biological replicates,  $N = 3$ . (H) RPA foci in indicated cells 24 hours after IR;  $N = 3$ ,  $n > 50$ , box-and-whisker plot shows median and 10th to 90th percentiles.  $*P = 0.0324$  [multiple-comparisons analysis of variance (ANOVA)].



(TUNEL) (Fig. 2B). Activation of the DNA damage response was noted by increased RPA association, ATR (ataxia telangiectasia and RAD3-related) association, and phosphorylation of histone variant H2AX (fig. S5, C to E). The DDR signaling from ICAD-tethered LacO arrays was dependent on CAD, as small interfering RNA (siRNA)-mediated knockdown of CAD reduced the recruitment of RPA and the phosphorylation of H2AX (Fig. 2C). Inhibition of caspase activity had no apparent effect on the recruitment of RPA to ICAD-tethered LacO arrays (fig. S5F). This demonstrates a capacity of CAD to mediate DNA break accumulation while associated with intact ICAD, independent of caspase signaling.

### CAD-dependent DNA breaks at defined genomic loci

Together, our observations indicate that CAD-dependent DNA breaks appear to predominantly manifest as SSBs. To determine whether these breaks were occurring at defined genomic loci, we mapped SSBs at base-pair resolution in HCT116 wild-type or CAD KO cells before, 20 min after, and 24 hours after IR by GLOE-seq (genome-wide ligation of 3'-OH ends followed by sequencing, fig. S6A) (24). Examining natural SSB frequency as a function of different chromatin states, we found a weak prevalence of SSBs at active enhancers and transcription initiation sites, known to be associated with accessible chromatin, as well as insulators as defined by CTCF binding (Fig. 2, D and E). CTCF has multiple functions in genome biology as it assists the three-dimensional (3D) folding of chromatin by regulating the location of chromatin loops formation (25). This SSB distribution was also maintained immediately after irradiation and was independent of the presence of CAD enzyme (Fig. 2D). However, 24 hours after irradiation, a more distinctive distribution was observed in the presence of wild-type but not CAD KO cells: SSBs concentrated more on insulator regions while becoming relatively depleted in heterochromatic regions (Fig. 2, D and E). This shift in pattern was entirely consistent among replicates (fig. S6B). Consistent with the chromatin state analysis, we also observed a high enrichment of SSBs at and around CTCF binding sites 24 hours after irradiation, in a CAD-dependent manner (Fig. 2E).

We sought to more precisely pinpoint the SSBs around CTCF sites at base-pair resolution, using the mapping information of the first read, which identifies the exact nick ligation site and strand. Piling up nick sites around CTCF binding sites revealed a periodic pattern (Fig. 2F and fig. S7, A and B), with nicks in the plus and minus strand being separated by 185 base pairs. Nucleosomes are known to be well positioned around CTCF sites (26); hence, we used published acetylated histone H3 and linker histone chromatin immuno-

precipitation sequencing (ChIP-seq) data to delineate the position of core and linker histones (27, 28). Matching GLOE-seq with these ChIP-seq patterns revealed a consistent periodicity of core, linker histone, and SSB, with SSBs arising symmetrically left and right of the linker histone footprint (Fig. 2F). This suggested that DNA bound by the nucleosomes and linker histone DNA is protected from SSBs. The nick was introduced in a strand-specific manner, with the plus strand being nicked on the "plus" side of the linker histone, and the minus strand on the "minus" side of the linker histone; this suggests a potential role for histones (or chromatin structure in general) in directing and orienting CAD activity in a strand-specific manner.

CAD-induced SSBs appeared to be less random than naturally occurring SSBs. We noted initially that multiple unique GLOE-seq reads tended to accumulate at relatively few sites in the genome at 24 hours after irradiation, but not in any other condition. Thus, we used an unbiased approach to quantify SSB hotspots (more than three unique SSBs mapped in close proximity on the same strand). Twenty-four hours after irradiation in wild-type but not CAD KO cells, we observed a statistically significant ( $P = 5.6 \times 10^{-5}$ ) factor of 2 increase across the three experimental replicates (Fig. 2G). A large number of the hypersensitivity sites that arose 24 hours after IR were new. We termed these CAD-dependent SSBs (CdSSBs), and they appeared to accumulate at hotspots different from those generally sensitive to occurrence of SSBs. Comparing wild-type and CAD KO cells 24 hours after irradiation, we observed 1371 unique pileups in wild-type cells, corresponding to putative CdSSBs, whereas ~581 unique pileups were present in the CAD KO but not wild-type cells (Fig. 2H). Notably, 232 of these 1371 CdSSBs overlapped with published CTCF peaks and 195 with DNase hypersensitive sites. Of the unique 581 pileups found in CAD KO cells, the overlap was only 11 and 14, respectively. In summary, genome-wide SSB mapping revealed a characteristic, unusual, CAD-dependent SSB landscape 24 hours after irradiation.

### DDR signaling through ICAD coordinates CAD activity after genotoxic stress

Next, we investigated whether CAD and ICAD are embedded in the DDR signaling machinery in response to genotoxic stress. To explore this, we examined the recruitment of CAD/ICAD to stripes of microirradiated DNA in real time. Here, we observed that both ICAD and CAD were recruited with comparable kinetics to subnuclear regions of DNA breaks (Fig. 3A and movies S1 and S2). Unexpectedly, we noted that ICAD could also be recruited to chromatin after IR in the absence of CAD, which could indicate that the recruitment of

CAD is mediated in part by ICAD after IR (fig. S8A). Examination of the recruitment to microirradiated DNA of a series of ICAD truncation fragments in ICAD-deficient cells indicated that all fragments could be recruited to irradiated regions. Fragments lacking the C-terminal domains of ICAD displayed a modest delay in accumulation (fig. S8, B to D). These results indicate that multiple regions of ICAD are responsible for chromatin recruitment.

Next, we examined whether a DDR signal could regulate the recruitment of CAD/ICAD to microirradiated stripes. We noted that inhibition or loss of ATM (ataxia telangiectasia mutated) and ATR kinase activity could limit the recruitment of CAD/ICAD (Fig. 3B and fig. S9, A to D). A similar role of the ATR kinase was also observed the day after IR, where ATR inhibition transiently diminished CAD chromatin recruitment as well as the corresponding number of DNA breaks (Fig. 3, C and D). To determine whether ATR regulates ICAD more directly, we analyzed the sequence of ICAD and identified two potential ATM/ATR phosphorylation sites, Ser<sup>107</sup> and Ser<sup>257</sup>, that are highly conserved across mammalian species (Fig. 3E). Further, the phosphorylation of Ser<sup>257</sup> on ICAD was previously identified in phosphoproteome analysis of human cells exposed to IR (29). We assessed the propensity of ATR to phosphorylate ICAD in vitro, and demonstrated that ICAD can be directly phosphorylated by ATR, dependent on the ICAD SQ sites (fig. S9E). To further address the biological relevance of ICAD phosphorylation, we generated phospho-specific antibodies toward the Ser<sup>107</sup> and Ser<sup>257</sup> sites. Both sites appeared extensively phosphorylated after cell exposure to IR, and the phosphorylation was dependent on both ATM and ATR kinase activity 24 hours after IR (Fig. 3F and fig. S9, F to I). Next, we expressed a serine-to-alanine mutant form of ICAD that could not be phosphorylated (S107A and S257A; DSA) to investigate the functional relevance of these phosphorylation events (Fig. 3F and fig. S9F). Measuring recruitment to microirradiated stripes of DNA damage demonstrated that the DSA variant could not be stably recruited to these sites, unlike the wild-type ICAD (Fig. 3G). In addition, the DSA variant could not completely restore RPA foci formation at 24 hours after IR even though expression of CAD was restored (Fig. 3H and fig. S9F). This indicates that the ATR/ATM-dependent phosphorylation of ICAD functionally contributes to regulating the induction of DNA breaks and continued control of the checkpoint through CAD/ICAD after IR.

### CAD is required for cell cycle checkpoint control and tumor cell survival after IR

Next, we investigated the role of CAD/ICAD-dependent maintenance of the G<sub>2</sub> cell cycle

checkpoint. We confirmed premature mitotic entry observed in the siRNA-based screen using individual siRNAs targeting CAD and ICAD and in the CAD-deficient KO cells (Fig. 4, A to C). This revealed that the breakdown in  $G_2$

checkpoint control in CAD-deficient cells was most pronounced 24 hours after IR, which corresponded with our observed peak of CAD-inflicted DNA breaks (Fig. 4, B and C). To further characterize the molecular basis of

the CAD/ICAD-dependent checkpoint regulation, we noted reduction of the inhibitory phosphorylation of cyclin-dependent kinase CDK1 (Tyr<sup>15</sup>), reduction in active checkpoint kinase CHK2, and moderate difference in

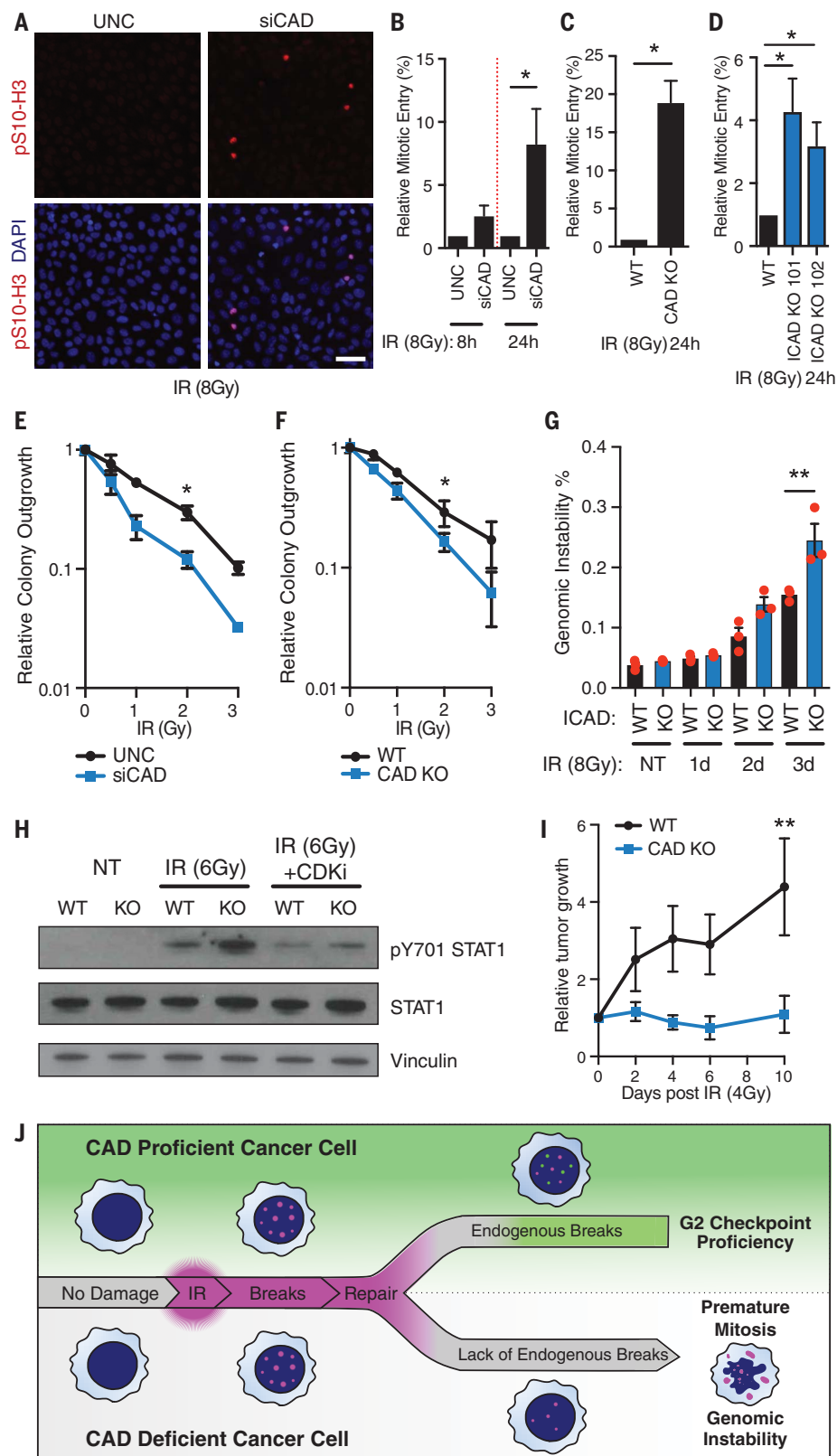


**Fig. 4. CAD/ICAD are required for tumor cell survival and checkpoint maintenance after IR.**

**(A)** Mitotic (pS10-H3) staining of irradiated and nocodazole (NZ)-trapped U2OS cells transfected with control siRNA (UNC) and siRNA against CAD. Cells were irradiated with 6 Gy of IR; after a 2-hour recovery, NZ was added for 8 hours before cells were fixed for immunofluorescence. Scale bar, 50  $\mu$ m. **(B)**  $G_2$  checkpoint maintenance in HCT116 CAD siRNA knockdown cells upon 8 Gy of IR. Data are means  $\pm$  SEM;  $N = 3$ . \* $P < 0.05$  (unpaired Student's  $t$  test). **(C)**  $G_2$  checkpoint maintenance in HCT116 CAD KO cells 24 hours after 8 Gy of IR. Data are means  $\pm$  SEM;  $N = 3$ . \* $P < 0.05$  (unpaired Student's  $t$  test). **(D)**  $G_2$  checkpoint maintenance in U2OS ICAD KO cells 24 hours after 6 Gy of IR. Data are means  $\pm$  SEM;  $N = 3$ . \* $P < 0.05$  (unpaired Student's  $t$  test). **(E)** Relative colony outgrowth of CAD-depleted cells after IR exposures. Data are means  $\pm$  SEM;  $N = 4$ . \* $P < 0.05$  (unpaired Student's  $t$  test). **(F)** Relative colony outgrowth of CAD KO HCT116 cells upon indicated IR exposure. Data are means  $\pm$  SEM;  $N = 4$ . \* $P < 0.05$  (unpaired Student's  $t$  test). **(G)** Genomic instability in U2OS WT and ICAD KO cells upon 8 Gy of IR. % Genomic instability represents total number of cells displaying micronuclei and fragmented nuclei divided by the total number of cells. Data are means  $\pm$  SEM;  $N = 3$ ,  $n > 400$ . \*\* $P = 0.0016$  (ANOVA). **(H)** Immunoblotting of pY701 STAT1 3 days after 6 Gy of IR in WT and ICAD KO cells. CDK1 inhibitor RO-3306 was added 2 hours after IR. **(I)** Normalized tumor growth of HCT116 WT and HCT116 CAD KO tumors after 4 Gy of IR. Data are means  $\pm$  SEM;  $n = 6$ . \*\* $P = 0.0055$  (two-way multiple-comparisons ANOVA). **(J)** Model of CAD-dependent  $G_2$  phase checkpoint.

active CHK1 (fig. S10, A to E). CDK1 inhibition is required to restrict mitotic entry after IR. Additionally, activated CHK2 and the phosphorylation of KAP1 have also been implicated in controlling mitotic entry of cells after IR (30). In line with our previous observations, this checkpoint function appeared independent from caspase signaling and unrelated to apoptotic cell death (fig. S11, A to C). Further, a CAD-promoted G<sub>2</sub> checkpoint was not observed in nonmalignant cells (fig. S11D), as normal cells harbor proficient p53 and pRB pathways that ensure robust G<sub>1</sub>/S transition control and diminished G<sub>2</sub> checkpoint dependency. The timing of G<sub>2</sub> checkpoint breakdown in CAD-deficient cancer cells corresponded to the kinetics of CAD-inflicted DNA breaks, indicating that this DNA modification may functionally prevent premature mitotic entry after IR. Notably, CAD/ICAD-deficient cells that entered mitosis prematurely exhibited a high number of lagging chromosomes and chromatin bridges (fig. S11E).

Aberrant cell cycle progression and premature mitotic entry with unrepaired DSBs leads to mitotic cell death, which contributes to radiosensitivity (21, 37). Indeed, cancer cells lacking the expression of CAD or ICAD displayed increased radiosensitivity (Fig. 4, E and F, and fig. S12A). This phenomenon was selective for cancer cells, as loss of CAD in nonmalignant cells had no impact (fig. S12B). Failure to repair DNA breaks through the inhibition of PARP activity has been suggested to sensitize cells to IR (32). Therefore, we examined whether failure to repair CAD-inflicted DNA breaks would contribute to this sensitization. We found that CAD-proficient cancer cells were sensitized to radiation by the addition of PARP inhibitor 24 hours after IR. However, PARP-inhibited CAD-deficient cells did not display any additional sensitization to IR (fig. S12C). Additionally, we noted that the loss of G<sub>2</sub> cell cycle checkpoint control led to the increased incidence of unstable nuclei (micronuclei and fragmented nuclei) (Fig. 4G and fig. S11E). Such genomic instability is considered to be a potent molecular pattern signal that activates inflammatory STAT1 signaling (33). Thus, we assessed the activating phosphorylation of STAT1 at Tyr<sup>701</sup> after IR in wild-type and CAD-deficient cells. This revealed elevated p-Tyr<sup>701</sup> STAT1 in CAD-deficient cells after IR, which was dependent on progression through mitosis (Fig. 4H). These observations are in line with recent research demonstrating that premature progression through mitosis after radiation promotes STAT1 signaling, and our data further indicate that CAD/ICAD limits this response (33, 34).

To complement the cell-based observations, we analyzed CAD function in a model of tumor radiotherapy in vivo, using human

tumor xenografts and tumor growth after radiation (Fig. 4I and fig. S12, D to F). Consistent with the cell-based survival assessment, a pronounced negative impact on tumor growth was detected after irradiation in tumors deficient in CAD, relative to their CAD-proficient counterparts. The irradiated CAD-deficient tumors demonstrated elevated p-Tyr<sup>701</sup> STAT1 compared to the wild-type tumors at endpoint (fig. S12G). Collectively, these results support the concept that the CAD-dependent pathway actively promotes cancer cell survival after IR. Previous murine studies had implicated CAD as a potential tumor suppressor, which was linked to pro-apoptotic function (10). However, analysis of gene expression data comparing normal and malignant tissues in human cancers indicated that loss of function of CAD/ICAD is a rare event (fig. S13, A and B) (35). Further, elevated expression of CAD in particular was noted in multiple tumor types (fig. S13, A and B)—an observation that is consistent with a potential, as yet unidentified, tumor-supporting role for CAD.

## Discussion

Together, our results unravel a DDR-mediated G<sub>2</sub> phase checkpoint pathway where cancer cells exposed to IR inflict reversible CAD-dependent DNA breaks including the CdSSBs. These lesions stimulate signaling responses and prevent premature mitotic entry (Fig. 4J), which enhances cancer cell survival. As repair of IR-induced DNA damage progresses, the number of highly genotoxic complex DNA DSBs declines, dropping below a threshold required to maintain the checkpoint. In turn, the induction of CAD-dependent DNA breaks signals an amplification of the DDR, further stabilizing the G<sub>2</sub> checkpoint and thereby providing more time for repair of the more complex, difficult-to-repair, and potentially lethal IR-induced genotoxic lesions.

The observations presented here indicate that the CAD-mediated checkpoint signal is primarily dependent on the generation of CdSSBs, a form of DNA damage characterized by rapid repair kinetics. Further, we implicate the activity of PARP-1 in the repair of CAD-mediated DNA breaks, as the addition of a nicotinamide adenine dinucleotide (NAD)-like PARP-1 inhibitor, 4-ANI, promotes DNA break formation in a CAD-dependent manner. Inhibition of PARP-1 activity has been reported to impair the G<sub>1</sub> checkpoint but enhance the G<sub>2</sub> checkpoint in irradiated cells (36), which may be the result of loss of PARP-1-directed repair of CdSSBs leading to increased DNA lesion burden. Furthermore, we uncovered an activating role of ICAD phosphorylation mediated by the DNA damage-induced ATM and ATR kinases. This may suggest an ongoing DNA damage-mediated feedback loop that is active until repair of complex lesions is completed, at

which stage the kinase signaling declines. In this regard, we note that multiple posttranslational modification sites have been identified in ICAD ([www.phosphosite.org/proteinAction.action?id=9541&showAllSites=true](http://www.phosphosite.org/proteinAction.action?id=9541&showAllSites=true)). These additional sites suggest that multiple signaling events may converge to regulate the CAD/ICAD checkpoint pathway.

Prior observations had established a temporally delayed secondary wave of SSBs after IR; however, the origin and functional role of these lesions have remained obscure. We identified CdSSBs as the source of these lesions, which accumulate at a subset of CTCF sites in the genome. These genomic loci may be accompanied by a moderate number of CAD-dependent stochastic lesions that escape detection because of rare targeting events within unspecified regions. Functionally, CTCF sites serve as binding domains for the CTCF protein, which regulates 3D chromosomal looping and topologically associated domains (TADs) in interphase cells (25). In response to positioned DSBs, chromosomal loops form in proximity to the CTCF sites, which act to sculpt the chromatin spreading of the phosphorylated histone variant  $\gamma$ H2AX. Given that CdSSBs extend cell cycle checkpoint control, an appealing concept is that the newly formed SSBs help to enforce a chromatin response to DNA damage. This is supported by the CAD-dependent phosphorylation of KAP1, a major chromatin marker of ongoing DDR. Here, CAD nuclease activity is restricted to generate CTCF-directed SSBs after IR, which is in contrast to CAD-dependent genome-wide intranucleosomal cleavage events during apoptosis. Hence, the precision of strand break formation may be a determinant in how CAD guides cancer cell survival.

On the basis of our present study, we propose that CAD/ICAD signaling is an adaptive cancer-intrinsic mechanism to resist genotoxic stress. The apparent selectivity of this stress-tolerance pathway likely reflects multiple factors that occur in cancer but not normal cells, including defects in the p53 and pRB pathways controlling G<sub>1</sub>/S transition, oncogene-driven premature S-phase entry, enhanced replication stress, and defective DNA repair, as well as checkpoint signaling mechanisms. The CAD/ICAD-mediated pathway may reflect adaptation to the genome-destabilizing selective pressures during tumorigenesis and contribute to therapy resistance. Such a prosurvival checkpoint pathway also reveals a cancer-selective vulnerability, thereby providing a potential avenue to enhance tumor cell radiosensitivity by targeting this G<sub>2</sub> cell cycle checkpoint.

## REFERENCES AND NOTES

1. R. A. Sharma et al., *Nat. Rev. Clin. Oncol.* **13**, 627–642 (2016).
2. T. D. Halazonetis, V. G. Gorgoulis, J. Bartek, *Science* **319**, 1352–1355 (2008).



3. M. T. Dillon, J. S. Good, K. J. Harrington, *Clin. Oncol.* **26**, 257–265 (2014).
4. A. Cieślak-Pobuda, Y. Saenko, J. Rzeszowska-Wolny, *Mutat. Res.* **732**, 9–15 (2012).
5. D. K. Klein et al., *Nat. Commun.* **6**, 5800 (2015).
6. A. N. Kousholt et al., *J. Cell Biol.* **197**, 869–876 (2012).
7. M. Enari et al., *Nature* **391**, 43–50 (1998).
8. K. Samejima, W. C. Earnshaw, *Nat. Rev. Mol. Cell Biol.* **6**, 677–688 (2005).
9. R. A. V. Bell, L. A. Megeney, *Cell Death Differ.* **24**, 1359–1368 (2017).
10. B. D. Larsen, C. S. Sørensen, *FEBS J.* **284**, 1160–1170 (2017).
11. J. H. Song, K. Kandasamy, M. Zemskova, Y. W. Lin, A. S. Kraft, *Cancer Res.* **71**, 506–515 (2011).
12. J. D. Orth, A. Loewer, G. Lahav, T. J. Mitchison, *Mol. Biol. Cell* **23**, 567–576 (2012).
13. X. Liu et al., *Cell Res.* **27**, 764–783 (2017).
14. G. Ichim et al., *Mol. Cell* **57**, 860–872 (2015).
15. B. D. Larsen et al., *Proc. Natl. Acad. Sci. U.S.A.* **107**, 4230–4235 (2010).
16. J. S. Brown, B. O’Carrigan, S. P. Jackson, T. A. Yap, *Cancer Discov.* **7**, 20–37 (2017).
17. J. Murai et al., *Cancer Res.* **72**, 5588–5599 (2012).
18. X. Li et al., *J. Biol. Chem.* **282**, 36177–36189 (2007).
19. M. H. Al-Khalaf et al., *Cell Discov.* **2**, 15041 (2016).
20. V. Iglesias-Guimaraes et al., *J. Biol. Chem.* **288**, 9200–9215 (2013).
21. R. G. Syljuåsen et al., *Cancer Res.* **64**, 9035–9040 (2004).
22. H. Sakahira, Y. Takemura, S. Nagata, *Arch. Biochem. Biophys.* **388**, 91–99 (2001).
23. S. M. Janicki et al., *Cell* **116**, 683–698 (2004).
24. A. M. Sriramachandran et al., *Mol. Cell* **78**, 975–985.e7 (2020).
25. C. Arnould, G. Legube, *J. Mol. Biol.* **432**, 724–736 (2020).
26. Y. Fu, M. Sinha, C. L. Peterson, Z. Weng, *PLOS Genet.* **4**, e1000138 (2008).
27. S. Walz et al., *Nature* **511**, 483–487 (2014).
28. C. M. Torres et al., *Science* **353**, aaf1644 (2016).
29. S. Matsuoka et al., *Science* **316**, 1160–1166 (2007).
30. H. Jaiswal et al., *EMBO J.* **36**, 2161–2176 (2017).
31. L. Galluzzi et al., *Cell Death Differ.* **25**, 486–541 (2018).
32. A. Dréan, C. J. Lord, A. Ashworth, *Crit. Rev. Oncol. Hematol.* **108**, 73–85 (2016).
33. S. M. Harding et al., *Nature* **548**, 466–470 (2017).
34. J. Chen et al., *Cell Rep.* **32**, 108080 (2020).
35. A. R. Cortazar et al., *Cancer Res.* **78**, 6320–6328 (2018).
36. M. Masutani, T. Nozaki, K. Wakabayashi, T. Sugimura, *Biochimie* **77**, 462–465 (1995).

## ACKNOWLEDGMENTS

We thank the core facilities at BRIC for assistance; the CSS laboratory for insightful comments; A. H. Lund (Biotech Research and Innovation Centre, University of Copenhagen) for HCT116 p53 KO cells; D. Spector (Cold Spring Harbor Laboratory) for U2OS 263 cells; D. Durocher (Lunenfeld-Tanenbaum Research Institute) for mCherry-LacR expression plasmid; F. Zhang (McGovern Institute, Massachusetts Institute of Technology) for pSpCas9(BB)-2A-GFP and pSpCas9(BB)-2A-GFP plasmids; W. Earnshaw (Wellcome Centre for Cell Biology, University of Edinburgh) for murine CAD/ICAD coexpression plasmid (pRHS); and B. Singers Sørensen (University of Aarhus) for discussions and cell lines used during revision. **Funding:** Supported by Danish Cancer Society grants R90-A5949 (C.S.S.), R204-A12415 (J.Be.), and R204-A12617-B153 (J.Ba.); Danish Council for Independent Research grant 4004-00621 (C.S.S.); Novo Nordisk Foundation grants NNF16OC0022358 (C.S.S.) and NNF 0060590 (J.Ba.); Canadian Institute of Health Research grant 156120 (L.A.M.); a postdoctoral grant from Independent Research Fund Denmark (B.D.L.); Czech Science Foundation grant 19-07674S and Swiss National Science Foundation grant 310030\_184716 (P.J.); Swedish Research council grant VR-MH 2014-46602-117891-30, Danish National Research Foundation (project CARD) grant DNRF 125, and Grant Agency of the Czech Ministry of Health grant NU21-03-00195 (J.Ba.); The

European Union’s Horizon 2020 program under the Marie Skłodowska-Curie grant (agreement 722729) (G.P.); and the Karolinska Institutet SFO for Molecular Biosciences, Vetenskapsrådet Junior Researcher grant 2015-04815, and H2020 ERC Starting Grant 715024 RAPID (S.J.E.). Bioinformatics analyses were performed on resources provided by the Swedish National Infrastructure for Computing (SNIC) at Uppmax server (projects SNIC 2020/15-9, SNIC 2020/6-3 to S.J.E.). **Author contributions:** Conceptualization: B.D.L., C.S.S. Methodology: B.D.L., J.Be., P.Y.K.Y., R.B., G.P., S.J.E., C.S.S. Experimental work: B.D.L., J.Be., P.Y.K.Y., R.B., G.P., V.U., J.K.A., T.T.K., S.E. Data documentation: B.D.L., J.Be., R.B., G.P., S.J.E., C.S.S. Data interpretation: B.D.L., J.Be., P.J., L.A.M., S.J.E., J.Ba., C.S.S. Funding acquisition: B.D.L., J.Be., P.J., L.A.M., S.J.E., J.Ba., C.S.S. Project administration: B.D.L., C.S.S. Supervision: B.D.L., P.J., L.A.M., S.J.E., J.Ba., C.S.S. Writing—original draft: B.D.L., J.Be., C.S.S. Writing—review and editing: B.D.L., J.Be., P.Y.K.Y., R.B., L.A.M., S.J.E., J.Ba., C.S.S. **Competing interests:** The authors declare that they have no competing interests. **Data and materials availability:** All materials are available upon request from C.S.S. All sequencing data and code are available at [www.ncbi.nlm.nih.gov/geo/query/acc.cgi?acc=GSE171242](http://www.ncbi.nlm.nih.gov/geo/query/acc.cgi?acc=GSE171242) and <https://doi.org/10.5281/zenodo.6386176>.

## SUPPLEMENTARY MATERIALS

[science.org/doi/10.1126/science.abi6378](https://doi.org/10.1126/science.abi6378)  
Materials and Methods  
Figs. S1 to S13  
Tables S1 and S2  
Movies S1 and S2  
References (37–44)  
MDAR Reproducibility Checklist

[View/request a protocol for this paper from Bio-protocol.](#)

30 March 2021; resubmitted 4 January 2022  
Accepted 30 March 2022  
10.1126/science.abi6378